ACS APPLIED MATERIALS & INTERFACES

Research Article

www.acsami.org

Activation of Organic Photovoltaic Light Detectors Using Bend Leakage from Optical Fibers

Matthew J. Griffith,*[,†] Matthew S. Willis,[†] Pankaj Kumar,[‡] John L. Holdsworth,[†] Henco Bezuidenhout,[§] Xiaojing Zhou,[†] Warwick Belcher,[†] and Paul C. Dastoor[†]

[†]Centre for Organic Electronics, University of Newcastle, University Drive, Callaghan, NSW 2308, Australia

[‡]CSIR-National Physical Laboratory, New Delhi, 110012, India

[§]AEL Mining Services Ltd, 1 Platinum Drive, Modderfontein, Johannesburg, 1645, South Africa

ABSTRACT: This work investigates the detection and subsequent utilization of leaked light from bends in a silica optical fiber using organic photovoltaic detectors. The optic power lost by single mode and multimode silica optical fibers was calibrated for bend radii between 1 and 7 mm for 532 and 633 nm light, exhibiting excellent agreement with previous theoretical solutions. The spatial location of maximum power leakage on the exterior of the fiber was found to exist in the same plane as the fiber, with a 10° offset from the normal. Two different organic photovoltaic detectors fabricated using a poly(3-hexylthiophene):indene-C_{60}-bisadduct donor–acceptor blend cast from chloroform and chlorobenzene were fabricated to detect the leaked light. The two detectors exhibited different photovoltaic performances, predominantly due to different active layer thicknesses. Both devices showed sensitivity to leakage light, exhibiting voltages between 200 and 300 mV in response to leaked light from the fiber. The temporal responses of the devices were observed to differ, with a rise time from 10% to 90% of maximum voltage of 1430 μs for the chlorobenzene device, and a corresponding rise time of 490 μs for the higher performing chloroform device. The two OPVs were used to simultaneously detect leaked light from induced bends in the optical fiber, with the differing temporal profiles employed to create a unique time-correlated detection signal with enhanced security. The delay between detection of each OPV voltage could be systematically varied, allowing for either a programmable and secure single detection signal or triggering of multiple events with variable time resolution. The results reported in this study present exciting avenues toward the deployment of this simple and noninvasive optical detection system in a range of different applications.

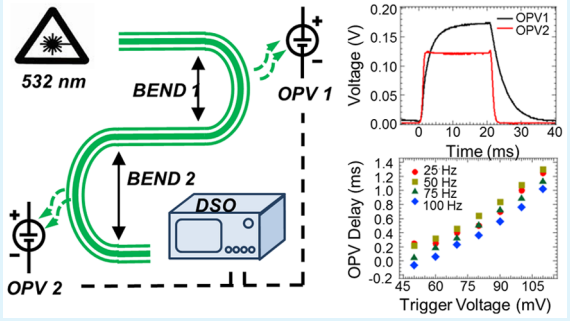

KEYWORDS: *bend leakage, optical fiber, organic photovoltaic cell, photodetector, polymer*

INTRODUCTION

The development of a low cost method to couple optical input signals to electronic detection units has great potential to advance current sensing technology in a range of different applications. Optical fiber waveguides have become a popular medium for sensing applications due to advantages such as high sensitivity, immunity to electromagnetic interference, and safety benefits in explosive or chemically unstable environments.[1] These benefits have led to the development of fiber optic sensors embedded within materials and systems that are able to measure a variety of parameters, including temperature, vibration, deformation, and strain, in real time and through a nondestructive evaluation.[2] However, current technologies often rely on light scattering mechanisms within the fiber to relay information, presenting a challenge in developing mechanisms that allow key sensing parameters to be determined at any point along an optical fiber with an appropriate sensitivity and spatial resolution, but within acceptable time limits.[3] This can require complicated components and high precision mounting at the input and output ends of an optical waveguide in order to obtain the highly sensitive signal, or coupling the signal to further circuitry for processing.[4] Consequently, optical sensing technologies are often reserved for expensive or high precision applications.

One way to circumvent the need for complex detection mechanisms would be to use the natural signal loss from bends in the optical fiber pathway. Loss of power at a bend in an optical fiber is an inherent feature of the nature of light propagation in a waveguide.[5] Such bend losses arise because light in the outer core and cladding must travel around a bend at a faster speed than the light in the center of the core in order to maintain a wavefront that is perpendicular to the direction of propagation.[6] The bend loss phenomenon has been thoroughly examined, and is typically considered to be a negative aspect of optical fiber sensors as it decreases the power available to perform the desired function.[7−9] However, there are a number

Received: December 18, 2015
Accepted: February 19, 2016
Published: February 19, 2016

DOI: 10.1021/acsami.5b12373
ACS Appl. Mater. Interfaces 2016, 8, 7928−7937

of reports which have examined utilizing the inherent bend loss of fibers as a diagnostic tool. Most common is the use of fiber Bragg gratings which selectively reflect wavelengths of light to determine the curvature of the light beam traveling down the fiber.[10−12] This approach can help detect and eliminate bend losses in systems where such effects are undesirable. Other practical applications of bend loss power attenuation include chemical sensors,[13,14] a related technology to measure the fluid level in a vessel,[15] and devices to detect strain[16] and temperature[17] changes at specific points on the fiber. Such applications have also been extended into the medical community, including a respiratory probe to analyze breathing irregularities[18] and an orthopedic sensor to study plantar pressure by analyzing the change in bend loss power which arises when a network of fibers are displaced by the physical deformation of an impinging foot.[19]

Given the breadth of applications using bend loss as an interrogation technique, it is somewhat surprising that there is a lack of technologies employing the light lost from the fiber to provide additional information, trigger external processes, or harvest energy. Standard photodiodes and detectors employed to interrogate the light pulses in optical fiber applications typically employ inorganic semiconductors which exhibit attractive functionalities such as high carrier mobility and high absorption coefficients; but they suffer from drawbacks such as high temperature synthesis, complex device fabrication methods, and low flexibility.[20,21] Operating in an unbiased photovoltaic mode, such detectors display response times in the order of 1−10 μs,[22] although they are typically employed in reverse biased photoconductive modes where the response times can be reduced to the order of 1 ns or lower for rapid response applications.[23,24] An emerging low cost alternative to these inorganic devices are organic semiconductors. Organic photovoltaic cells (OPVs), polymer-based devices which generate electricity directly from sunlight,[25] are ideal candidates for detectors of this leaked light with the potential to trigger external circuitry from their photogenerated voltage responses. The key advantage of OPVs is that the polymer blend materials, which are closely related to common plastics, can be printed at high speeds across large areas using roll-to-roll processing techniques.[26] Furthermore, OPV devices show excellent sensitivity to reduced and diffuse light levels such as those leaking from a fiber bend,[27] with response times in the range of 10−1000 ns under load,[28,29] although such response times rise considerably when operating in unbiased photovoltaic modes due to relatively low carrier mobility values. The high sensitivity allows the optical input signal leaked from the fiber bends to be easily detected with low cost components that can simultaneously provide timing signals, trigger multiple events with excellent time resolution, and could potentially power an entire detector unit using energy harvested from the leaked input light. The low cost nature of OPV technology is particularly useful for disposable sensor applications where cost is a major consideration.

In this work we investigate the potential to detect and utilize light leaked from bends in an optical fiber using OPV photodetectors. The ability to control the voltage output of the OPV detectors by modulating the bend radius of the fiber is examined, and the temporal resolution of the detector response is examined. Furthermore, we report on the development of a unique and secure trigger signal with a variable timing delay that can be created using the correlated voltage outputs from multiple OPVs. The results obtained from this work demonstrates both a proof of principle for a simple, low cost optical fiber sensing and signaling system, and also present the potential for adapting this system for a range of different applications in the future.

EXPERIMENTAL SECTION

OPV Fabrication. Prepatterned ITO-coated glass substrates (Xinyan Technologies, R_{sheet} < 15 Ω□$^{-1}$) were cleaned via successive sonication in detergent, deionized water, and isopropanol for 10 min each. Cleaned electrodes were then exposed to a UV-ozone treatment for 15 min. ITO substrates were then transferred to a thermal evaporation chamber where a 15-nm layer of molybdenum oxide was deposited at 0.15 Å s^{-1} at a base pressure of 2 × 10^{-6} mbar. Active layer blend solutions composed of poly(3-hexylthiophene) (P3HT) and indene-C_{60}-bisadduct (ICBA) in a ratio of 1:0.8 wt % (P3HT/ICBA) with a total blend concentration of 18 mg mL^{-1} were prepared using both chloroform and chlorobenzene as solvents. Active layers were deposited onto the oxide transport layer in a glovebox by spin coating at 2000 rpm for 60 s. Samples were subsequently cured at 60 °C for 5 min and then transferred to an evaporation chamber where a 20-nm calcium layer (evaporated at 0.6 Å s^{-1}) and a 130-nm aluminum layer (evaporated at 2 Å s^{-1}) were coated onto the active layer through a shadow mask, which defined the active area of the cells to be 14 mm^2 for the chloroform devices and 0.05 mm^2 for the chlorobenzene devices. The device architecture is shown in Figure 1. After fabrication, the OPV devices were transferred to a glovebox where they were annealed at 160 °C for 5 min before performance evaluation.

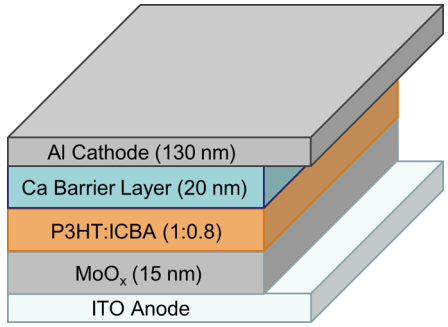

Figure 1. Architecture of the organic photovoltaic detectors employed in this study.

J−V and EQE Testing. Current density−voltage (J−V) measurements were performed using a Newport Class A solar simulator with an AM 1.5 spectrum filter. The light intensity was calibrated to 100 mW cm^2 using a silicon reference solar cell (FHG-ISE). J−V data were recorded in the dark and under illumination with a Keithley 2400 source meter. Individual devices were masked to an illuminated area of 3.8 mm^2 to eliminate additional photocurrent responses from neighboring devices on the common substrate. External quantum efficiency measurements were recorded by illuminating devices with a tungsten halogen lamp passed through an Oriel Cornerstone 130 monochromator. An Ithaco Dynatrac 395 analogue lock-in amplifier and Thorlabs PDA55 silicon diode were employed to collect the reference signal, and a Stanford Research Systems SR830 DSP digitizing lock-in amplifier was employed to measure the device current. The photoresponse of OPV devices to variations in incident light intensity was determined by illuminating the active area of devices with the frequency doubled 532-nm output from a Lambda-Pro Nd:YAG diode pumped solid state continuous wave laser through various neutral density filters.

Optical and Atomic Force Microscopy. Optical microscopy images of OPV active layers were obtained using a Zeiss Axioplan 2 microscope illuminated with a tungsten lamp. A 40× objective lens was used to focus though the device onto the active layer, with images subsequently captured with an Olympus DP70 CCD camera. Atomic

DOI: 10.1021/acsami.5b12373
ACS Appl. Mater. Interfaces 2016, 8, 7928−7937

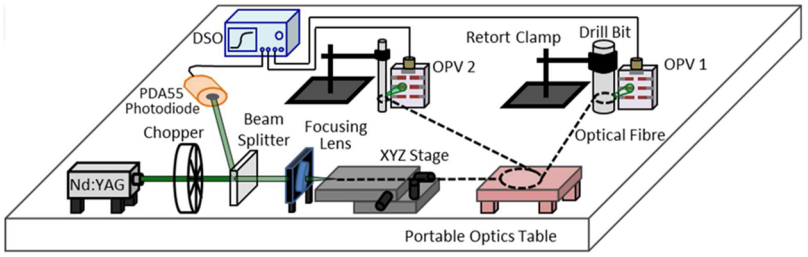

Figure 2. Schematic diagram of the experimental apparatus used to capture the OPV temporal response to light leaked from induced bends in an optical fiber.

force microscopy (AFM) images were collected using an Asylum Research Cypher in AC mode. A 300Al-G aluminum-coated silicon tip (Budget Sensors) with a resonant frequency of 300 kHz and a force constant of 40 N m^{-1} was employed to acquire all images over a sample area of 400 μm^2.

Scanning Transmission X-ray Microscopy. Samples were prepared for scanning transmission X-ray microscopy (STXM) by spinning onto low stress silicon nitride windows with silicon dioxide coating (window dimensions 0.25 × 0.25 mm^2, window thickness 15 nm, frame 5 × 5 mm^2). Pristine films of P3HT and fullerene acceptor were also prepared for near-edge X-ray absorption fine structure (NEXAFS) experiments. Profilometry (KLA Tencor Alpha-step 500) was used to confirm that the film thickness was ∼50 nm, as expected for monolayer coverage of these films.

STXM measurements were performed at the Advanced Light Source on beamline 5.3.2.[30] The STXM instrument has a theoretical resolution of 25 nm with a 31-nm spot size. The sample was mounted with the X-ray beam at normal incidence and the sample was then rastered with respect to the beam to form an image at a given specific beam energy. The sample chamber was backfilled with 0.33 atm of helium gas and was isolated from the synchrotron ring and beamline optics via a silicon nitride window. The transmitted X-ray beam was detected by a scintillator and a photomultiplier tube. The energy of the X-ray beam was varied between 284.4 and 287.4 eV, which covered the carbon K-shell to molecular orbital transitions with maximum X-ray contrast between the polymer and fullerene acceptor. Compositional maps were derived from images collected at 284.4 eV.

Optical Fiber Bend Leakage Calibration. The frequency doubled 532-nm output from a Lambda-Pro Nd:YAG diode pumped solid state continuous wave laser and the 633-nm output from a Melles-Griot HeNe laser were employed as light sources. The maximum power of the 532- and 633-nm lasers were determined to be 12 and 6 mW, respectively, using a Newport 840C optical power meter connected to an 833-SL (visible spectrum) photodiode calibrated with an OD3 neutral density filter. Single mode fiber with a core diameter of 2.5 μm (Thorlabs, 460 HP) and multimode fiber with a core diameter of 105 μm (Thorlabs, FG105LCA) were employed as light transmission media. The jacket coating was stripped from the ends using Clauss CFS-2 fiber strippers, with the exposed edges then cleaved to 90° using a Fitel S323 fiber cleaving unit (Furukawa Electric Company).

The cleaved fiber edges were coupled with the laser light sources using an AMA009/M fiber launching XYZ stage with micrometer resolution in each of the 3 spatial dimensions. Melles-Griot lenses were employed to focus the incident light within the cone of acceptance for each fiber prior to to the XYZ launching stage. Power attenuation calibration was performed by bending the coupled fiber into circular loops around metal cylinders with radii between 1 and 7 mm, then monitoring the power output from the fiber prior to and following the introduction of the bend. The angular dependence of the leaked optical power was determined by mounting the 840C power meter photodiode on a calibrated RP01/M rotating optical platform (Thorlabs). The diode was mounted 4 mm from the fiber, masked with a 4-mm^2 aperture, then rotated in a hemispherical plane around the fiber in 5° increments. The entire platform was then rotated by 90° and the process was repeated to capture angular dependence in a second perpendicular plane. Angular variation data were repeated in triplicate for each plane.

OPV Temporal Response Measurements. A square wave pulse was introduced into the incident light by directing it through a model 9479 mechanical chopper (EG&G Brookdeal) with a maximum chopping frequency of 900 Hz. The temporal resolution of the pulsed signal was determined by reflecting a portion of the light from a beam splitter onto a biased PDA55 silicon photodiode (ThorLabs, 10 MHz bandwidth at 0 dB gain). The chopped signal exhibited significant high frequency noise around the peak value, which was subsequently removed through the application of a smoothening binomial algorithm in Igor Pro (version 6.35A). This algorithm employs a Gaussian filter, convolving the measured signal with normalized coefficients derived from Pascals triangle at the tenth level. Application of this smoothening filter removed the high frequency noise, however, the spectral shape of the data remained unchanged. This shape was confirmed by plotting the smoothened data overlaid onto the raw photodiode data.

The remainder of the light from the beam splitter was directed into the fiber coupling apparatus and then onto the OPV detectors through leakage from induced bends in the fiber pathway. The OPV detectors were fixed in place using customized spring loaded clamps. A RIGOL DS4024 digital storage oscilloscope (DSO) averaging 128 scans was employed to record the responses of the photodiode and two OPV detectors. The experimental setup is shown schematically in Figure 2. Data recording was triggered from the leading edge of the laser square wave pulse (∼5% of the saturation value) with OPV temporal responses recorded at several different chopping frequencies.

RESULTS AND DISCUSSION

Analysis of Optical Fiber Bend Leakage. The degree of optical power attenuation at 532 and 633 nm resulting from the introduction of macrobends with various radii into the single and multimode fiber pathway is shown in Figure 3. Careful attention was paid to ensuring the coupling geometry was not modified throughout data collection for a particular wavelength and fiber, as this geometry was observed to strongly influence the attenuation loss down the fiber (caused by a change in the launch angle influencing the value of the propagation constant, β_g). The bend loss behavior shows a logarithmic dependence of the attenuation on the bend radius for both single mode and multimode fiber, as predicted from an analytical consideration of macrobending losses in cylindrical waveguides.[31] At visible wavelengths, several thousand modes pass down the multimode fiber and thus theoretical analysis of the attenuation loss requires advanced computational methods. However, for the single mode fibers with only the fundamental LP01 mode propagating, the theoretical loss was easily computed from the fundamental bend loss equation originally derived in ref 31 using fiber parameters of NA = 0.130, n_1 = 1.461 and n_2 = 1.451 at 532 and 633 nm respectively,[32] with the propagation constants determined using standard numerical techniques for straight fiber.[33] The experimental attenuation losses for both

DOI: 10.1021/acsami.5b12373
ACS Appl. Mater. Interfaces 2016, 8, 7928−7937

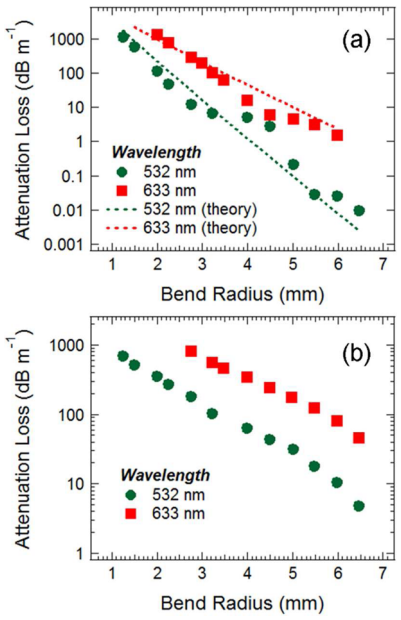

Figure 3. Attenuation loss per unit length caused by a single circular bend in a (a) single mode and (b) multimode silica optical fiber plotted against the radius of the bend. The dashed lines in (a) show the bend loss predicted from ref 31.

wavelengths show close agreement with the theoretical values. Furthermore, the measured attenuation exhibits no deviation from the pure logarithmic relationship of the bend loss equation such as the superimposed peaks that have been observed in similar studies at longer wavelengths.[34] This indicates the loss behavior in these materials at visible wavelengths is dominated by pure bending phenomena, and other pathways such as whispering gallery mode losses do not require consideration.[35,36]

The slope of the attenuation loss curves in Figure 3 is 2−2.5 times greater for the single mode fiber (0.33 dB mm^{-2} at 532 nm and 0.45 dB mm^{-2} at 633 nm) compared to the multimode fiber (0.13 dB mm^{-2} at 532 nm and 0.20 dB mm^{-2} at 633 nm). Thus, it is much more difficult to leak a predetermined target level of optical power from the single mode fiber due to a much lower tolerance in the bend radii values which will produce a leaked power close to the target. Therefore, a sensor device designed to function by detecting a calibrated level of power leakage is more suited to integration with a multimode fiber. Additionally, the power loss down the fiber was determined to be greater at 633 nm for all bend radii in both single and multimode fibers. This is somewhat unexpected as the loss in optical fibers is typically lower at longer wavelengths due to Rayleigh scattering. However, manufacturer's data indicates a slightly higher (∼10%) absorption in the silica matrix at 633 nm due to the peak of the NBOHC defect, a value that is consistent with the trends in the measured data when projected backward to a zero bend radius.[37] Indeed, all bend radii tested showed a loss of greater than 3 dB at 633 nm, which indicates that more than 50% of the incident power is lost. If light leakage from the fiber bends is employed to trigger detectors, it is clearly not possible to trigger the same magnitude of response in multiple devices if more than half the light is lost at any single bend. Considering this issue, and noting that optical signals can be transmitted across greater distances using 532 nm light, the multimode fiber guiding 532 nm light is determined to be the most suitable signal transmission method. This pairing of light source and transmission medium was therefore employed in all remaining experiments.

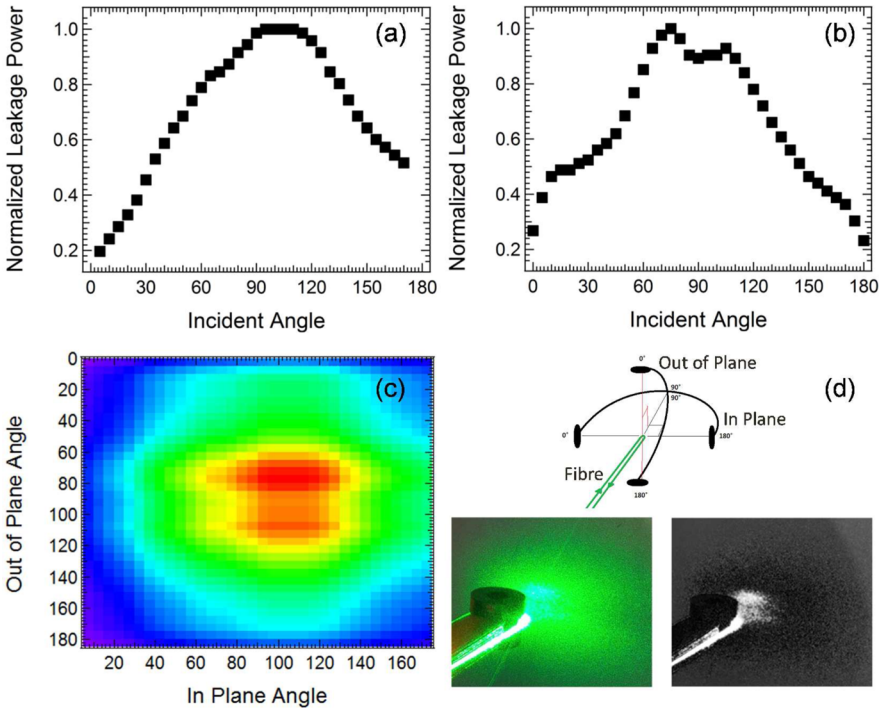

Figure 4. Change in optical power at 532 nm leaked from the multimode fiber with variation of the (a) in-plane angle and (b) out-of-plane angle. (c) A 2D construction of the power variation using the angular dependence measured in (a) and (b). (d) Schematic illustration of the measurement plane geometries and color and greyscale photographs of light leakage from a fiber bend.

DOI: 10.1021/acsami.5b12373
ACS Appl. Mater. Interfaces 2016, 8, 7928−7937

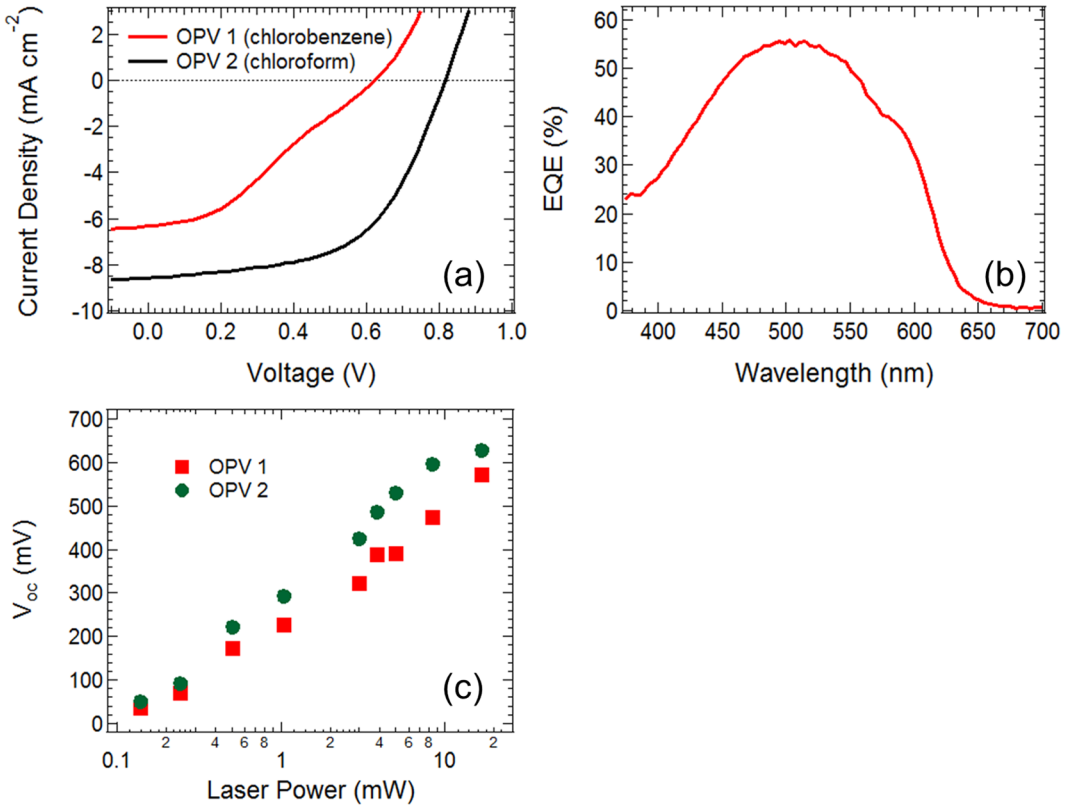

Figure 5. (a) Current density−voltage curves for OPV detectors with active layers spun from chlorobenzene (OPV 1) and chloroform (OPV 2). (b) EQE curve measured for OPV 1. (c) Dependence of open circuit voltage on the illumination intensity at 532 nm for OPV 1 and OPV 2.

The variation in the leaked optical power at different spatial locations outside the fiber bend was also investigated in order to determine the optimum position to couple a photosensor to the leaked light. Figure 4 shows the dependence of optical power leaked from the fiber with a bend radius of 3.25 mm as a function of angular variation in two perpendicular hemispherical planes. Data collected in the same plane as the fiber segments approaching and receding the bend is referred to as in-plane, while data collected in a plane perpendicular to the bend in the fiber is referred to as out-of plane. The 90° angle was set to be the line of the incoming fiber segment (in-plane measurements), or the plane of the incoming and outgoing fiber segments (out-of-plane).

The in-plane data show an approximately Gaussian dependence on the angular variation, with a peak at 100° and a fwhm of 135° (Figure 4a). The out-of-plane data show similar behavior, with a peak centered at 90° and a fwhm of 120° (Figure 4b). In the latter case the peak is split, with two distinct maxima appearing at 75° and 105° and the loss data appearing to dip slightly in between these values. This behavior is not an artifact, and was verified by examining a photograph of the light leaked from the fiber, which closely matches the projected 2-dimensional intensity map of the leaked light power (Figure 4c and 4d). From these data the spatial location of the maximum leaked light intensity can be easily obtained. This maximum, located slightly above the 2-D plane containing the fiber bend and with a 10° offset with respect to the central axis of the semicircular bend the incident fiber, is therefore the best place to position a photosensor in order to obtain maximum sensitivity.

Characterization of OPV Photodetectors. The photovoltaic performance of the OPV detectors prepared using two different active layer solvents is shown in Figure 5. Devices fabricated from cholorobenzene (labeled OPV 1) exhibit a short circuit current density of J_{sc} = 6.33 mA cm^{-2}, an open circuit voltage of V_{oc} = 625 mV, a fill factor of 0.328, and a power conversion efficiency of η = 1.30%. In contrast, the devices prepared from chloroform (labeled OPV 2) exhibit much higher performance, with all parameters of J_{sc} = 8.57 mA cm^{-2}, V_{oc} = 817 mV, a fill factor of 0.563, and subsequent η = 3.94% exhibiting increases compared to OPV 1. It is noted that these performance differences are not consistent with previous reports suggesting device efficiency is typically higher when the active layer solvent is chlorobenzene instead of chloroform.[38−40] The differences observed for the devices prepared here are, however, consistent with the fabrication conditions employed in these experiments as will be discussed shortly. These conditions were deliberately selected to produce a greater resistance in one device compared to the other by slightly altering the active area of each device for optimal use as photodetectors, rather than to maximize the power conversion efficiency of devices for optimal performance as energy conversion devices. This difference in series resistance, confirmed to be a factor of ∼6 by comparing the different slopes of the J−V curves around open circuit (Figure 5a), ensures a different characteristic time response between devices, which can be useful as an inherent timing mechanism when multiple OPV detectors are employed to detect leaked light from the fiber.

The external quantum efficiency (EQE) curve of the chlorobenzene device is shown in Figure 5b. The spectrum mirrors the known absorption spectrum of the P3HT polymer component,[25] showing broad conversion of absorbed light into free charges between 400 and 650 nm with a peak conversion at

DOI: 10.1021/acsami.5b12373
ACS Appl. Mater. Interfaces 2016, 8, 7928−7937

503 nm. The EQE curve in Figure 5b provides a frequency resolved indicator of the sensitivity of the device. Accordingly, it can be deduced from the EQE that OPV devices fabricated with a P3HT/ICBA active layer are ideally suited for detection of light at 532 nm, exhibiting a near maximum photon-to-current conversion efficiency of 53.4% at this wavelength. The photoresponse of the OPV detectors as a function of incident light intensity was also monitored (Figure 5c). Both OPV detectors show a similar logarithmic dependence of the photovoltage on light intensity at 532 nm, with OPV 1 exhibiting a slope of 252 mV per decade and OPV 2 exhibiting a slope of 297 mV per decade. The OPV sensor response shown in Figure 5c coupled with the bend leakage intensity calibration data in Figure 3 and angular dependence in Figure 4 therefore collectively quantify the expected photovoltage generated by the OPV sensor in response to light leaked from the fiber. The fraction of integrated power contained within the solid angle subtended by the sensor active area on the hemisphere of leaked light measured in Figure 4 can be adjusted for the known proportion of light leaked from a fiber of defined bend radius from Figure 3. After consideration of the coupling efficiency of the fiber to the laser source, which is approximately 50% for these measurements, the amount of light striking the sensor as a fraction of the incident laser power can be determined. Figure 5c can then be employed to convert this light intensity to an expected photovoltage response. For a sensor placed 4 mm from the fiber bend and a laser power of 10 mW, an optical power of ~360 μW is expected to strike the OPV detectors, leading to predicted photovoltages of 125 mV for OPV 1 and 170 mV for OPV 2.

The morphology of the active layer in devices spun from chloroform and chlorobenzene solvents were analyzed with optical microscopy, atomic force microscopy (AFM), and scanning transmission X-ray microscopy (STXM) to further understand the differences in device performance for samples prepared from the two solvents. The optical microscopy images (Figure 6a and 6b) show both films are homogeneous, displaying minimal large aggregates or fullerene clusters. This observation is consistent with the similar and relatively high solubilities of fullerene adducts in both chloroform and chlorobenzene.[41] It was noted that the chlorobenzene film appears much lighter in the optical images, indicative of a thinner film. Measurement of the film thickness verified this feature, finding thicknesses of 125 nm for the chloroform sample and 63 nm for the chlorobenzene sample. The AFM images of the sample surfaces shown in Figure 6c and 6d also showed great similarities. The AFM roughness of the chloroform sample appears to vary more strongly in the color contrast images, which may indicate slightly larger voids, however, given the scale of the variations is only between 0 and 10 nm, both films can be concluded to exhibit very smooth topology. RMS roughness values were determined to be 1.1 nm for the chlorobenzene sample and 1.7 nm for the chloroform sample, indicating that differences in surface topology are unlikely to be responsible for device performance differences. To further verify this conclusion, STXM images were acquired for blend films cast from each solvent at the Advanced Light Source. Because STXM is a transmission-based technique it is therefore an excellent tool to elucidate chemically selective information through the entire bulk thickness of the polymer blend layer. The large area maps were acquired at an energy of 284.4 eV where the fullerene acceptor absorbs strongly and the polymer has weak absorption. These STXM maps do not show

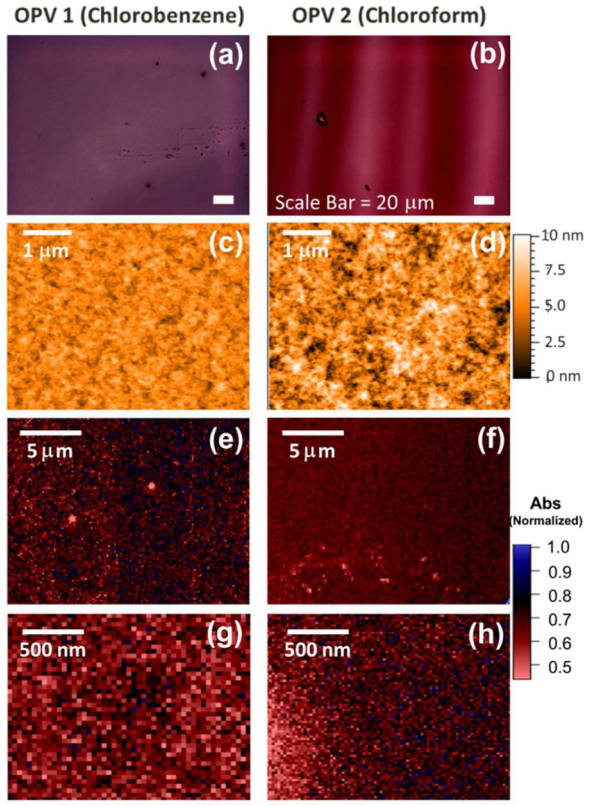

Figure 6. (a, b) Optical microscopy images, (c, d) atomic force microscopy images, (e, f) large area (20 μm × 20 μm) STXM images, and (g, h) high resolution (2 μm × 2 μm) STXM images of the P3HT/ICBA active layers spun from chlorobenzene (left) and chloroform (right).

any significant differences between the two films, with no large aggregates of either polymer or fullerene observed (Figure 6e and 6f). High resolution STXM maps acquired at the same energy show that blended films prepared from both solvents are uniformly and homogeneously mixed down to the scale of single pixels (Figure 6g and 6h); indicating that the morphology of films prepared in both solvents is indistinguishable down to the instrument resolution scale of 25 nm. Because the difference in observed device performance cannot be due to morphology, it is attributed to a combination of the different film thicknesses and series resistances of the devices. The fabrication conditions employed here have been previously optimized for chloroform based devices,[42] and use of the same parameters for active layer dissolved in chlorobenzene produces a thinner film as a larger fraction of the less volatile solvent is cast to the outer edges in the spin coating process. The film thickness of 125 nm produced from chloroform is therefore optimized for light harvesting as has been previously demonstrated from a consideration of optical interference effects in the device.[43] The film thickness of 63 nm is expected to produce a much lower photogenerated charge volume due to less photon absorption, and thus a lower photovoltage and photocurrent would be expected, exactly as observed. Furthermore, the greater series resistance of the chlorobenzene device will be expected to reduce both the short circuit current and the fill factor of the device in comparison to the chloroform device.

The temporal response of both OPVs to laser light was determined by passing the Nd:YAG source beam through a

DOI: 10.1021/acsami.5b12373
ACS Appl. Mater. Interfaces 2016, 8, 7928−7937

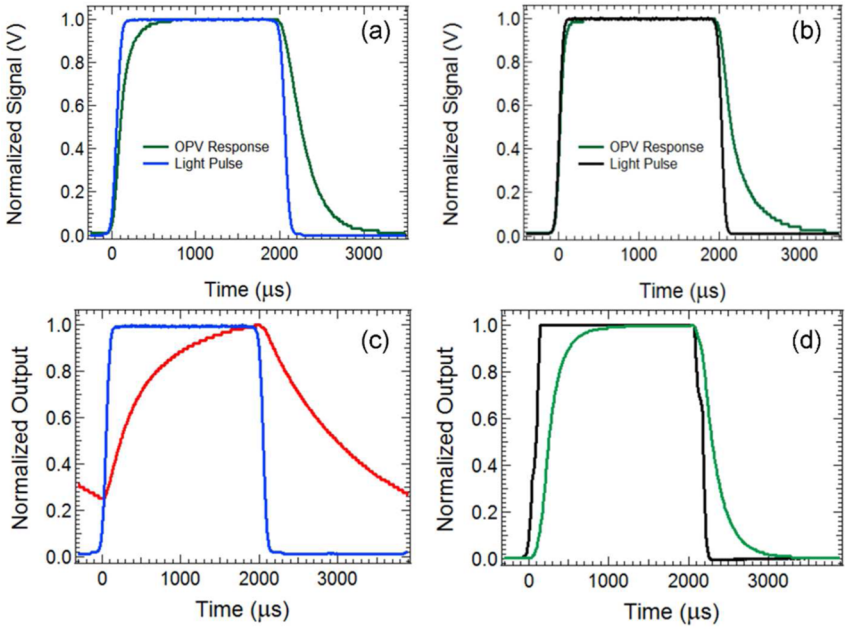

Figure 7. Temporal response of (a) OPV 1 and (b) OPV 2 to 532 nm illumination chopped at a frequency of 250 Hz. The temporal response of (c) OPV 1 and (d) OPV 2 to 532 nm leaked from a bend in a silica multimode fiber of radius 3 mm. Light launched into the fiber was also chopped at a frequency of 250 Hz.

mechanical chopper to induce temporal variations into the signal. Figure 7a and 7b show the responses of OPV 1 (chlorobenzene) and OPV 2 (chloroform) under open circuit conditions to illumination with 532 nm light chopped at a frequency of 250 Hz. The temporal resolution of the equipment, including the chopped optical pulses and the photodiode response, was determined by monitoring the 10−90 rise time, which is the time required for the signal to rise from 10% of its saturation voltage to 90% of this value. For a chopping frequency of 250 Hz, this resolution was determined to be 108 μs and is dominated by the chopping mechanism, as the blades take a finite time to pass through the beam to block and unblock its passage to the photodiode. In comparison, the 10−90 rise times of the OPVs were determined to be 246 μs for OPV1 and 118 μs for OPV 2. These time responses represent the convolution of the instrument response with the true OPV temporal response. Accurate deconvolution of the intrinsic OPV response remains an area of ongoing investigation, however, a more accurate estimate of the intrinsic OPV response was obtained by systematically increasing the chopping frequency until the respective OPV time responses reached constant values, indicating the temporal resolution of the equipment was no longer influencing the OPV response. Under these conditions, a chopping frequency of 900 Hz produced an equipment resolution of 32 μs, with the plateau OPV 10−90 rise times determined to be 190 μs for OPV 1 and 80 μs for OPV 2. It is apparent that the temporal response of the high performance OPV 2 is faster than that of the low performance OPV 1 by a factor of 2.4. Earlier analysis of the active layer found that the blended polymer film is thinner by a factor of 2 for the slower OPV 1, suggesting that charge transport through the films is less likely to be the cause of the differing response times. Instead, it was noted earlier that the series resistance of the chlorobenzene device was ∼6 times higher than that of the chloroform device. The interfacial area of the chloroform device was 2.8 times larger than that of the chlorobenzene device, leading to a similar enlargement of the capacitance of the device as it scales linearly with area. The RC time constant of the chlorobenzene device is thus expected to be higher than that of the chloroform device by a factor of ∼2.2, very close to the observed difference. Furthermore, since both blends are lightly doped p-type semiconductors, they will be entirely depleted at thicknesses of 60−130 nm, suggesting that changes in the depletion width will not influence the time response of these photodetectors. The built-in potentials of the devices are also expected to be very similar, since this difference arises from the work function offsets of the electrodes or interface layers, which are identical for each device. The different V_{oc} values, often used as an indicator of the built-in potential, in this case simply reflect different charge densities at open circuit due to the previously discussed difference in film thickness leading to different photon absorption profiles. Given these considerations, it appears that the difference in response times of the two photodetectors is dominated by the RC time constant of the films. This feature is highly advantageous in that it introduces the potential to control the response times by simply altering the sensor fabrication conditions to vary the device resistance or capacitance.

Utilizing Multiple OPVs Photodetectors for Enhanced Temporal Response and Signal Security. Detection of light leaked from the optic fiber bends using the two different OPV detectors was subsequently investigated by fixing them in space with respect to the fiber bends using custom-built sample holders. The OPVs were placed at open circuit condition in the same plane as the fiber, with a 10° offset from the normal as this was determined to be the position of maximum leaked light intensity from the data in Figure 4. Figure 7c and 7d show the responses of OPV 1 (chlorobenzene) and OPV 2 (chloroform), respectively, to 532 nm light chopped at a frequency of 250 Hz and leaked from circular bends of radius 3 mm in a silica multimode optical fiber. Again, the chlorobenzene cast OPV1 was observed to respond to sensitizing light slower than the chloroform cast OPV2. The 10−90 rise times for the devices were 1430 μs for OPV1 and 490 μs for OPV 2. These values

DOI: 10.1021/acsami.5b12373
ACS Appl. Mater. Interfaces 2016, 8, 7928−7937

are 6−8 times slower than the native responses observed for direct laser illumination of the OPV detectors in Figure 7a and 7b, indicating a time delay in light leaking out of the fiber bends onto the detectors. The raw voltage signals prior to normalization were in the range of 200−300 mV, significantly larger than the detection limit for an OPV device. This result therefore verifies that organic photovoltaic devices can indeed be utilized in applications requiring the detection of light by simply introducing a bend into the fiber path rather than employing expensive and complicated detectors coupled into the fiber directly.

In addition to detecting the leaked light, the differing temporal responses of the two OPV detectors can also be utilized advantageously to create a unique detection signal by introducing a simple comparator circuit with a programmable time window between detectable events. Given the different temporal responses of the two OPV devices, when both are employed on bends of the same optical fiber simultaneously the rise to maximum voltage occurs with different temporal slopes (Figure 8a). If a specified voltage level must be surpassed to trigger a positive detection event, then the different rise times of the two OPV devices ensure there will be a time delay between the faster and slower OPVs reaching this voltage trigger level. Furthermore, this time delay can be deliberately varied by judicious choice of the trigger voltage, since the different temporal responses of the two detectors cause the rising voltages to diverge in the time domain as the trigger voltage is increased (Figure 8b). When the system was arranged in the configuration shown in Figure 2, with a bend of radius 10 mm employed for OPV 1, followed by a bend of radius of 3 mm for OPV2, the voltage responses shown in Figure 8a were obtained. Varying the voltage trigger threshold between 50 and 110 mV produces delays between detection of the faster OPV 2 and the slower OPV1 of 0.1−1.2 ms. Thus, at maximum voltage (where both OPVs can be detected), a time difference of 1.2 ms can be detected from OPV devices with a difference in RC time constants of 2.4. Altering the RC time constants of the devices by changing the fabrication conditions or device area would then be expected to lead to time delays which are altered by a similar factor. Therefore, a calibrated time delay of any desired value can be specified between detection of the two voltage peaks generated by the OPV detectors under illumination, making it unlikely that the detector assembly will respond positively to false stimuli; imparting a significant signal security component to the detection system.

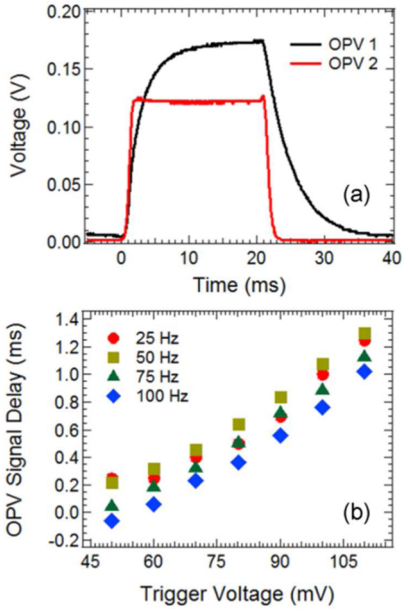

Figure 8. (a) Temporal response of the two OPV detectors to light leaked from induced bends in a multimode fiber after chopping at a frequency of 25 Hz. (b) Variation in the delay between OPV photovoltage detection as the desired trigger level is varied between 50 and 110 mV at different chopping frequencies.

The timing mechanism created using the differing temporal responses of two different OPV detectors produces time delays of 0.1−1.2 ms between detection events. As discussed above, this can be utilized to create a secure detection signal for a signal event, or could potentially be utilized to trigger two separate events with a time resolution in the range of hundreds of microseconds. To reduce the time delay between detection of threshold voltages for the two OPV detectors, both voltage signals were acquired from the same OPV device. The first 10-mm radius bend in the fiber was directed to leak light onto one finger of the higher performing OPV2, while the second 3-mm radius bend directed the leaked light onto a second finger of the same OPV2 device. This setup removes the differences in the temporal responses of the device that previously generated the time delay between detection of voltage thresholds from each sensor. However, provided the leaked light levels onto each finger of the same OPV sensor are slightly different, the maximum voltage generated by each sensor will also be different. Consequently, the two OPV devices have voltage slopes which are slightly diverging in time, since the slopes rise at the same rate but to different maximum levels (Figure 9a). This arrangement of detectors can be utilized to produce a much finer control of the time delay between voltage threshold detection for the two OPV fingers than was earlier observed when employing two different OPV devices. Indeed, Figure 9b

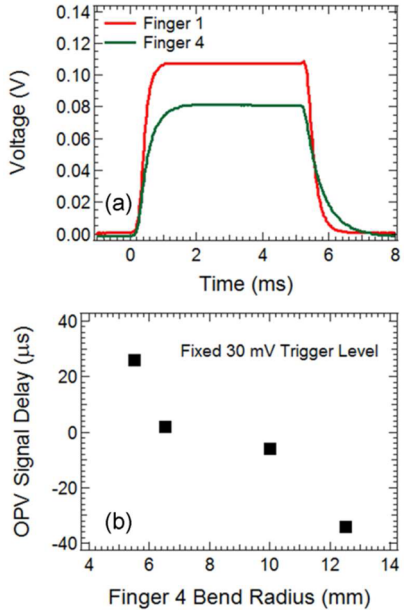

Figure 9. (a) Temporal response of two different fingers connected in parallel on OPV 2 to light leaked from induced bends in a multimode fiber after chopping at a frequency of 25 Hz. (b) Variation in the delay between OPV photovoltage detection as the desired trigger level is varied between 50 and 110 mV at different chopping frequencies.

DOI: 10.1021/acsami.5b12373
ACS Appl. Mater. Interfaces 2016, 8, 7928−7937

demonstrates that the time delay between detection of the nominated trigger voltage for each OPV sensor can be varied systematically from −30 us (Finger 4 detected first) to +30 μs (Finger 1 detected first). This encouraging result suggests that the time delay between OPV voltage detection can be controlled on a much finer time scale, allowing the current detection system to trigger events from light input signals with a time resolution on a time scale of 1−10 μs. This result offers exciting potential for the deployment of this simple optical sensing system in a range of different applications.

CONCLUSIONS

This work has successfully demonstrated that light signals launched into optical waveguides can be easily detected using organic photovoltaic devices by simply introducing a bend into the fiber path and sensitizing the OPV devices with the leaked light. This arrangement provides a simple low-cost approach for signal detection in optical fiber directly. The optical power at 532 and 633 nm leaked from silica single mode and multimode optical fibers was calibrated in response to a range of different bend radii. Data for the single mode fiber displayed excellent fits to the standard Marcuse bend loss formula, suggesting that this formula can be employed to extend the calibration beyond the limited range of bending radii measured in this study. The spatial location of maximum power leakage on the exterior of the fiber was carefully probed, and found to exist in the same plane as the fiber, with a 10° offset from the normal. Two OPV detectors were prepared to detect the leaked light, each cast from different solvents. The device cast from chlorobenzene showed relatively poor performance, while that cast from chloroform showed excellent device performance. The difference between the device performances appeared to be dominated by the thickness of the active layer, which was well below the optimal value for the chlorobenzene device and therefore influenced the current that could be generated.

It was demonstrated that the OPV detectors could successfully detect light leaked from the multimode optical fiber, exhibiting maximum open circuit voltages of 200−300 mV for the input laser power of 10 mW coupled to the fiber. The temporal responses of the devices were observed to differ, with a rise time from 10% to 90% of maximum voltage of 1430 μs observed for the chlorobenzene device, and a corresponding rise time of 490 μs for the higher performing chlorobenzene device. The two OPVs were used to simultaneously detect leaked light from induced bends in the optical fiber, however, given their different temporal response characteristics, there was a delay between the times each OPV recorded a set voltage trigger level. This delay can potentially be used as a predefined detection condition for additional signal security, or alternatively, can represent the minimum time resolution for triggering multiple events. A minimum time delay of 1−10 μs was achieved by utilizing two of the six fingers on the same OPV device. The results reported in this study present exciting avenues toward the deployment of this simple and noninvasive optical sensing system in a range of different applications.

AUTHOR INFORMATION

Corresponding Author

*E-mail: matthew.griffith@newcastle.edu.au.

Notes

The authors declare no competing financial interest.

ACKNOWLEDGMENTS

We gratefully acknowledge both the assistance of and useful discussions with Dr A. L. D. Kilcoyne regarding acquisition and analysis of STXM data at the Advanced Light Source. This research was funded by AEL Mining Services Ltd through an industry partnership agreement. This work was performed in part at the Materials node of the Australian National Fabrication Facility, which is a company established under the National Collaborative Research Infrastructure Strategy to provide nano and microfabrication facilities for Australia's researchers. P.K. acknowledges funding support by INSA New Delhi for allowing a travelling fellowship at the University of Newcastle.

REFERENCES

(1) Lomer, M.; Arrue, J.; Jauregui, C.; Aiestaran, P.; Zubia, J.; López-Higuera, J. M. Lateral Polishing of Bends in Plastic Optical Fibres Applied to a Multipoint Liquid-Level Measurement Sensor. *Sens. Actuators, A* **2007**, *137*, 68−73.

(2) Measures, R. N. *Structural Monitoring with Fiber Optic Technology*, 1st ed.; Academic Press: San Diego, CA, 2001.

(3) Bao, X.; Chen, L. Recent Progress in Distributed Fiber Optic Sensors. *Sensors* **2012**, *12*, 8601−8639.

(4) Wang, X.-D.; Wolfbeis, O. S. Fiber-Optic Chemical Sensors and Biosensors (2008−2012). *Anal. Chem.* **2013**, *85*, 487−508.

(5) Boechat, A. A. P.; Su, D.; Hall, D. R.; Jones, J. D. C. Bend Loss in Large Core Multimode Optical Fiber Beam Delivery Systems. *Appl. Opt.* **1991**, *30*, 321−327.

(6) Senior, J. M. *Optical Fibre Communications: Principles and Practice*, 3rd ed.; Pearson Education Limited: Essex, England, 2009.

(7) Jay, J. A. *An Overview of Macrobending and Microbending of Optical Fibers*; White Paper WP1212; Corning Incorporated, 2010.

(8) Baggett, J. C.; Monro, T. M.; Furusawa, K.; Finazzi, V.; Richardson, D. J. Understanding Bending Losses in Holey Optical Fibers. *Opt. Commun.* **2003**, *227*, 317−335.

(9) Olszewski, J.; Szpulak, M.; Martynkien, T.; Urbanczyk, W.; Berghmans, F.; Nasiłowski, T.; Thienpont, H. Analytical Evaluation of Bending Loss Oscillations in Photonic Crystal Fibers. *Opt. Commun.* **2007**, *269*, 261−270.

(10) Kuang, K. S. C.; Cantwell, W. J.; Scully, P. J. An Evaluation of a Novel Plastic Optical Fibre Sensor for Axial Strain and Bend Measurements. *Meas. Sci. Technol.* **2002**, *13*, 1523−1534.

(11) Shao, L.-Y.; Laronche, A.; Smietana, M.; Mikulic, P.; Bock, W. J.; Albert, J. Highly Sensitive Bend Sensor with Hybrid Long-Period and Tilted Fiber Bragg Grating. *Opt. Commun.* **2010**, *283*, 2690−2694.

(12) Liu, Y.; Williams, J. A. R.; Bennion, I. Optical Bend Sensor Based on Measurement of Resonance Mode Splitting of Long-Period Fiber Grating. *IEEE Photonics Technol. Lett.* **2000**, *12*, 531−533.

(13) López, R. M.; Spirin, V. V.; Shlyagin, M. G.; Miridonov, S. V.; Beltrán, G.; Kuzin, E. A.; Marquez Lucero, A. Coherent Optical Frequency Domain Reflectometry for Interrogation of Bend-Based Fiber Optic Hydrocarbon Sensors. *Opt. Fiber Technol.* **2004**, *10*, 79−90.

(14) Sai, V. V. R.; Kundu, T.; Mukherji, S. Novel U-Bent Fiber Optic Probe for Localized Surface Plasmon Resonance Based Biosensor. *Biosens. Bioelectron.* **2009**, *24*, 2804−2809.

(15) Lomer, M.; Quintela, A.; López-Amo, M.; Zubia, J.; López-Higuera, J. M. A Quasi-Distributed Level Sensor Based on a Bent Side-Polished Plastic Optical Fibre Cable. *Meas. Sci. Technol.* **2007**, *18*, 2261−2267.

(16) Kiesel, S.; Peters, K.; Hassan, T.; Kowalsky, M. Behaviour of Intrinsic Polymer Optical Fibre Sensor for Large-Strain Applications. *Meas. Sci. Technol.* **2007**, *18*, 3144−3154.

(17) Peters, K. Polymer Optical Fiber Sensors - a Review. *Smart Mater. Struct.* **2011**, *20*, 13002.

DOI: 10.1021/acsami.5b12373
ACS Appl. Mater. Interfaces 2016, 8, 7928−7937

(18) Raza, A.; Augousti, A. T. Optical Measurement of Respiration Rates. In *Proceedings of the Seventh Conference on Sensors and their Applications*, 1995, Dublin, Ireland; CRC Press; pp 325−330.
(19) Wang, W.-C.; Ledoux, W. R.; Sangeorzan, B. J.; Reinhall, P. G. A Shear and Plantar Pressure Sensor Based on Fiber-Optic Bend Loss. *J. Rehabil. Res. Dev.* **2005**, *45*, 315−326.
(20) Game, O.; Singh, U.; Kumari, T.; Banpurkar, A.; Ogale, S. ZnO(N)−Spiro-MeOTAD Hybrid Photodiode: An Efficient Self-Powered Fast-Response UV (visible) Photosensor. *Nanoscale* **2014**, *6*, 503−513.
(21) Pavesi, L.; Lockwood, D. J.; *Silicon Photonics*, Vol. *1*; Springer-Verlag: Berlin, Germany, 2004.
(22) Pernot, C.; Hirano, A.; Iwaya, M.; Detchprohm, T.; Amano, H.; Akasaki, I. Solar-Blind UV Photodetectors Based on GaN/AlGaN p-i-n Photodiodes. *Jpn. J. Appl. Phys.* **2000**, *39*, L387−L389.
(23) Colace, L.; Balbi, M.; Masini, G.; Assanto, G.; Luan, H.-C.; Kimerling, L. C. Ge on Si p-i-n Photodiodes Operating at 10 Gbit/s. *Appl. Phys. Lett.* **2006**, *88*, 101111.
(24) Matsuo, K.; Teich, M. C.; Saleh, B. E. A. Noise Properties and Time Response of the Staircase Avalanche Photodiode. *J. Lightwave Technol.* **1985**, *6*, 1223−1231.
(25) Günes, S.; Neugebauer, H.; Sariciftci, N. S. Conjugated Polymer-Based Organic Solar Cells. *Chem. Rev.* **2007**, *107*, 1324−1338.
(26) Hösel, M.; Krebs, F. C. Large-Scale Roll-to-Roll Photonic Sintering of Flexo Printed Silver Nanoparticle Electrodes. *J. Mater. Chem.* **2012**, *22*, 15683−15688.
(27) Koster, L. J. A.; Mihailetchi, V. D.; Ramaker, R.; Blom, P. W. M. Light Intensity Dependence of Open-Circuit Voltage of Polymer:-Fullerene Solar Cells. *Appl. Phys. Lett.* **2005**, *86*, 123509.
(28) Philippa, B.; Stolterfoht, M.; Burn, P. L.; Juška, G.; Meredith, P.; White, R. D.; Pivrikas, A. The Impact of Hot Charge Carrier Mobility on Photocurrent Losses in Polymer-Based Solar Cells. *Sci. Rep.* **2014**, *4*, 5695.
(29) Sagmeister, M.; Tschepp, A.; Kraker, E.; Abel, T.; Lamprecht, B.; Mayr, T.; Köstler, S. Enabling Luminescence Decay Time-Based Sensing Using Integrated Organic Photodiodes. *Anal. Bioanal. Chem.* **2013**, *405*, 5975−5982.
(30) Kilcoyne, A. L. D.; Tyliszczak, T.; Steele, W. F.; Fakra, S.; Hitchcock, P.; Franck, K.; Anderson, E.; Harteneck, B.; Rightor, E. G.; Mitchell, G. E.; Hitchcock, A. P.; Yang, L.; Warwick, T.; Ade, H. Interferometer-Controlled Scanning Transmission X-ray Microscopes at the Advanced Light Source. *J. Synchrotron Radiat.* **2003**, *10*, 125−136.
(31) Marcuse, D. Curvature Loss Formula for Optical Fibres. *J. Opt. Soc. Am.* **1976**, *66*, 216−220.
(32) Green, M. A.; Keevers, M. J. Optical Properties of Intrinsic Silicon at 300 K. *Prog. Photovoltaics* **1995**, *3*, 189−192.
(33) Marcuse, D. *Light Transmission Optics*; Van Nostrand Reinhold: New York, 1972.
(34) Wang, Q.; Farrell, G.; Freir, T. Theoretical and Experimental Investigations of Macro-Bend Losses for Standard Single Mode Fibers. *Opt. Express* **2005**, *13*, 4476−4484.
(35) Harris, A. J.; Castle, P. F. Bend Loss Measurements on High Numerical Aperture Single-Mode Fibers as a Function of Wavelength and Bend Radius. *J. Lightwave Technol.* **1986**, *4*, 34−40.
(36) Boleininger, A.; Lake, T.; Hami, S.; Vallance, C. Whispering Gallery Modes in Standard Optical Fibres for Fibre Profiling Measurements and Sensing of Unlabelled Chemical Species. *Sensors* **2010**, *10*, 1765−1781.
(37) Thorlabs Product Specification Sheet, FG105LCA Glass Clad Silica Multimode Optic Fibre (Low Hydroxyl). https://www.thorlabs.com/thorproduct.cfm?partnumber=FG105LCA, accessed 12 November 2015.
(38) Dang, M. T.; Wantz, G.; Bejbouji, H.; Urien, M.; Dautel, O. J.; Vignau, L.; Hirsch, L. Polymeric Solar Cells Based on P3HT:PCBM: Role of the Casting Solvent. *Sol. Energy Mater. Sol. Cells* **2011**, *95*, 3408−3418.
(39) Ruderer, M. A.; Guo, S.; Meier, R.; Chiang, H.-Y.; Körstgens, V.; Wiedersich, J.; Perlich, J.; Roth, S. V.; Müller-Buschba, P. Solvent-Induced Morphology in Polymer-Based Systems for Organic Photovoltaics. *Adv. Mater.* **2011**, *21*, 3382−3391.
(40) Kawano, K.; Sakai, J.; Yahiro, M.; Adachi, C. Effect of Solvent on Fabrication of Active Layers in Organic Solar Cells Based on Poly(3-Hexylthiophene) and Fullerene Derivatives. *Sol. Energy Mater. Sol. Cells* **2009**, *93*, 514−518.
(41) Kim, Y. S.; Lee, Y.; Kim, J. K.; Seo, E.-O.; Lee, E.-W.; Lee, W.; Han, S.-H.; Lee, S.-H. Effect of Solvents on the Performance and Morphology of Polymer Photovoltaic Devices. *Current Appl. Phys.* **2010**, *10*, 985−989.
(42) Xue, B.; Vaughan, B.; Poh, C.-H.; Burke, K. B.; Thomsen, L.; Stapleton, A.; Zhou, X.; Bryant, G. W.; Belcher, W.; Dastoor, P. C. Vertical Stratification and Interfacial Structure in P3ht:Pcbm Organic Solar Cells. *J. Phys. Chem. C* **2010**, *114*, 15797−15805.
(43) Nam, Y. M.; Huh, J.; Jo, W. H. Optimization of Thickness and Morphology of Active Layer for High Performance of Bulk-Heterojunction Organic Solar Cells. *Sol. Energy Mater. Sol. Cells* **2010**, *94*, 1118−1124.

DOI: 10.1021/acsami.5b12373
ACS Appl. Mater. Interfaces 2016, 8, 7928−7937